

Simscape Model - Nano Hexapod

Dehaeze Thomas

April 7, 2025

Contents

| | | |
|----------|---|-----------|
| 1 | Active Vibration Platforms | 4 |
| 1.1 | Sample Stages with Active Control | 4 |
| 1.2 | Active Vibration Platform | 7 |
| 2 | The Stewart platform | 9 |
| 2.1 | Mechanical Architecture | 9 |
| 2.2 | Kinematic Analysis | 10 |
| 2.3 | The Jacobian Matrix | 12 |
| 2.4 | Static Analysis | 15 |
| 2.5 | Dynamical Analysis | 16 |
| 3 | Multi-Body Model | 18 |
| 3.1 | Model Definition | 18 |
| 3.2 | Validation of the multi-body model | 20 |
| 3.3 | Nano Hexapod Dynamics | 21 |
| 4 | Control of Stewart Platforms | 24 |
| 4.1 | Centralized and Decentralized Control | 24 |
| 4.2 | Choice of the Control Space | 25 |
| 4.3 | Active Damping with Decentralized IFF | 27 |
| 4.4 | MIMO High-Authority Control - Low-Authority Control | 27 |
| | Bibliography | 32 |

Building upon the validated multi-body model of the micro-station presented in previous sections, this section focuses on the development and integration of an active vibration platform model.

A review of existing active vibration platforms is given in Section 1, leading to the selection of the Stewart platform architecture. This parallel manipulator architecture, described in Section 2, requires specialized analytical tools for kinematic analysis. However, the complexity of its dynamic behavior poses significant challenges for purely analytical approaches.

Consequently, a multi-body modeling approach was adopted (Section 3), facilitating seamless integration with the existing micro-station model.

The control of the Stewart platform introduces additional complexity due to its multi-input multi-output (MIMO) nature. Section 4 explores how the High Authority Control/Low Authority Control (HAC-LAC) strategy, previously validated on the uniaxial model, can be adapted to address the coupled dynamics of the Stewart platform. This adaptation requires fundamental decisions regarding both the control architecture (centralized versus decentralized) and the control frame (Cartesian versus strut space). Through careful analysis of system interactions and plant characteristics in different frames, a control architecture combining decentralized Integral Force Feedback for active damping with a centralized high authority controller for positioning was developed, with both controllers implemented in the frame of the struts.

1 Active Vibration Platforms

The conceptual phase started with the use of simplified models, such as uniaxial and three-degree-of-freedom rotating systems. These models were chosen for their ease of analysis, and despite their simplicity, the principles derived from them usually apply to more complex systems. However, the development of the Nano Active Stabilization System (NASS) now requires the use of a more accurate model that will be integrated with the multi-body representation of the micro-station. To develop this model, the architecture of the active platform must first be determined.

The selection of an appropriate architecture begins with a review of existing positioning stages that incorporate active platforms similar to NASS (Section 1.1). This review reveals two distinctive features of the NASS that set it apart from existing systems: the fact that the active platform is continuously rotating and its requirement to accommodate variable payload masses. In existing systems, the sample mass is typically negligible compared to the stage mass, whereas in NASS, the sample mass significantly influences the system's dynamic behavior.

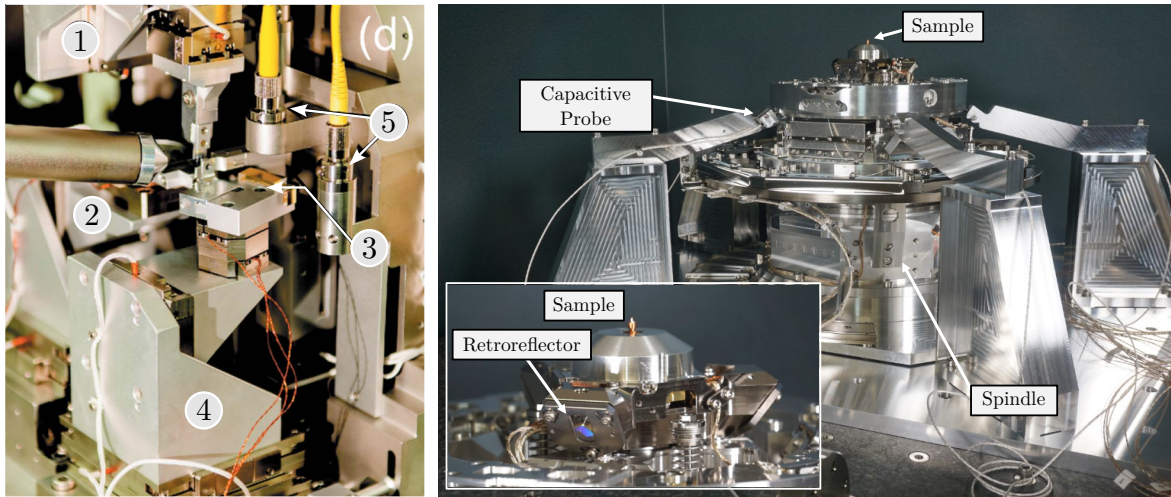
These distinctive requirements drive the selection of the active platform architecture. In Section 1.2, different active platform configurations, including serial and parallel configurations, are evaluated, ultimately leading to the choice of a Stewart platform architecture.

1.1 Sample Stages with Active Control

The positioning of samples with respect to X-ray beam, that can be focused to sizes below 100 nanometers, presents significant challenges, because mechanical positioning systems are typically limited to micron-scale accuracy. To overcome this limitation, external metrology systems have been implemented to measure sample positions with nanometer accuracy, enabling real-time feedback control for sample stabilization.

A review of existing sample stages with active vibration control reveals various approaches to implementing such feedback systems. In many cases, sample position control is limited to translational degrees of freedom. At NSLS-II, for instance, a system capable of 100 μm stroke has been developed for payloads up to 500g, utilizing interferometric measurements for position feedback (Figure 1.1a). Similarly, at the Sirius facility, a tripod configuration based on voice coil actuators has been implemented for XYZ position control, achieving feedback bandwidths of approximately 100 Hz (Figure 1.1b).

The integration of R_z rotational capability, which is necessary for tomography experiments, introduces additional complexity. At ESRF's ID16A beamline, a Stewart platform (whose architecture will be presented in Section 2) using piezoelectric actuators has been positioned below the spindle (Figure 1.2a). While this configuration enables the correction of spindle motion errors through 5-DoF control based on capacitive sensor measurements, the stroke is limited to 50 μm due to the inherent constraints of piezoelectric actuators. In contrast, at PETRA III, an alternative approach places a XYZ-stacked stage above the spindle, offering 100 μm stroke (Figure 1.2b). However, attempts to implement real-time

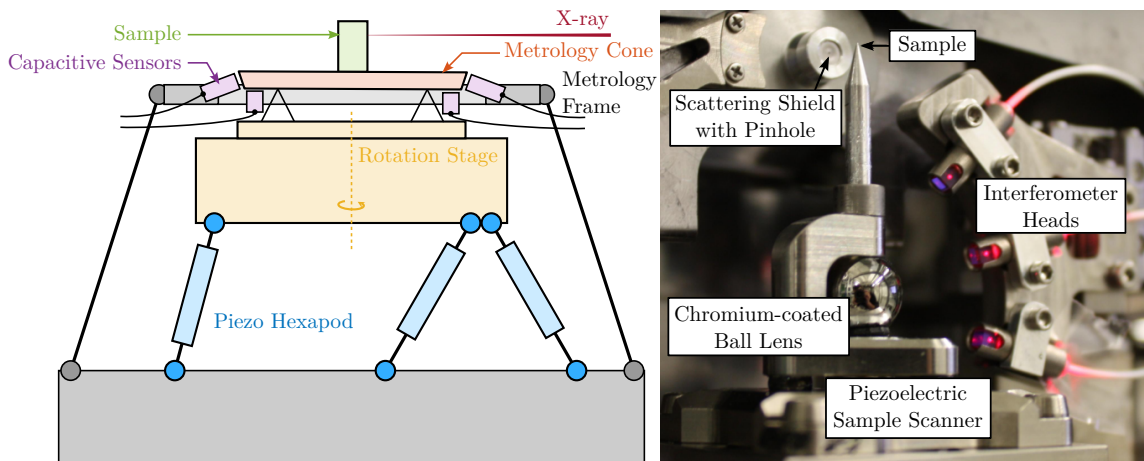


(a) MLL microscope

(b) SAPOTI sample stage

Figure 1.1: Example of sample stage with active XYZ corrections based on external metrology. The MLL microscope [1] at NSLS-II (a). Sample stage on SAPOTI beamline [2] at Sirius facility (b)

feedback using YZ external metrology proved challenging, possibly due to the poor dynamical response of the serial stage configuration.



(a) Simplified schematic of ID16a end-station

(b) PtyNAMi microscope

Figure 1.2: Example of two sample stages for tomography experiments. ID16a endstation [3] at the ESRF (a). PtyNAMi microscope [4], [5] at PETRA III (b)

Table 1.1 provides an overview of existing end-stations that incorporate feedback loops based on online metrology for sample positioning. Although direct performance comparisons between these systems are challenging due to their varying experimental requirements, scanning velocities, and specific use cases, several distinctive characteristics of the NASS can be identified.

The first key distinction of the NASS is in the continuous rotation of the active vibration platform.

Table 1.1: End-Stations with integrated feedback loops based on online metrology. The stages used for feedback are indicated in bold font. Stages not used for scanning purposes are omitted or indicated between parentheses. The specifications for the NASS are indicated in the last row.

| Stacked Stages | Specifications | Measured DoFs | Bandwidth | Reference |
|---|--|--|--------------------------|---------------------------------|
| Sample XYZ stage (piezo) | light $D_{xyz} : 0.05 \text{ mm}$ | Interferometers D_{xyz} | 3 PID, n/a | APS [1] |
| Sample Spindle Hexapod (piezo) | light $R_z : \pm 90 \text{ deg}$ $D_{xyz} : 0.05 \text{ mm}$ $R_{xy} : 500 \mu\text{rad}$ | Capacitive sensors D_{xyz}, R_{xy} | $\approx 10 \text{ Hz}$ | ESRF ID16a [3] |
| Sample XYZ stage (piezo) Spindle | light $D_{xyz} : 0.1 \text{ mm}$ $R_z : 180 \text{ deg}$ | Interferometers D_{yz} | n/a | PETRA III P06 [4], [5] |
| Sample Spindle Tripod (piezo) | light $R_z : \pm 182 \text{ deg}$ $D_{xyz} : 0.4 \text{ mm}$ | Interferometers D_{yz}, R_x | PID, n/a | PSI OMNY [6], [7] |
| Sample (XY stage) Spindle XYZ linear motors | light $R_z : 360 \text{ deg}$ $D_{xyz} : 0.4 \text{ mm}$ | Interferometers D_{xyz}, R_{xy} | n/a | Soleil Nanoprobe [8], [9] |
| Sample Spindle XYZ stage (piezo) | up to 0.5kg $R_z : 360 \text{ deg}$ $D_{xyz} : 0.1 \text{ mm}$ | Interferometers D_{xyz} | n/a | NSLS SRX [10] |
| Sample Parallel XYZ VC | up to 0.35kg $D_{xyz} : 3 \text{ mm}$ | Interferometers D_{xyz} | $\approx 100 \text{ Hz}$ | Diamond, I14 [11] |
| Sample Parallel XYZ VC (Spindle) | light $D_{xyz} : 3 \text{ mm}$ $R_z : \pm 110 \text{ deg}$ | Capacitive sensors and interferometers D_{xyz} | $\approx 100 \text{ Hz}$ | LNLS CARNAUBA [2] |
| Sample Active Platform (Micro-Hexapod) Spindle Tilt-Stage Translation Stage | up to 50kg $R_z : 360 \text{ deg}$ $R_y : \pm 3 \text{ deg}$ $D_y : \pm 10 \text{ mm}$ | D_{xyz}, R_{xy} | | ESRF ID31 [12], [13] |

This feature introduces significant complexity through gyroscopic effects and real-time changes in the platform orientation, which substantially impact both the system’s kinematics and dynamics. In addition, NASS implements a unique Long-Stroke/Short-Stroke architecture. In conventional systems, active platforms typically correct spindle positioning errors - for example, unwanted translations or tilts that occur during rotation, whereas the intended rotational motion (R_z) is performed by the spindle itself and is not corrected. The NASS, however, faces a more complex task: it must compensate for positioning errors of the translation and tilt stages in real time during their operation, including corrections along their primary axes of motion. For instance, when the translation stage moves along Y, the active platform must not only correct for unwanted motions in other directions but also correct the position along Y, which necessitate some synchronization between the control of the long stroke stages and the control of the active platform.

The second major distinguishing feature of the NASS is its capability to handle payload masses up to 50 kg, exceeding typical capacities in the literature by two orders of magnitude. This substantial increase in payload mass fundamentally alters the system’s dynamic behavior, as the sample mass significantly influences the overall system dynamics, in contrast to conventional systems where sample masses are negligible relative to the stage mass. This characteristic introduces significant control challenges, as the feedback system must remain stable and maintain performance across a wide range of payload masses (from a few kilograms to 50 kg), requiring robust control strategies to handle such large plant variations.

The NASS also distinguishes itself through its high mobility and versatility, which are achieved through the use of multiple stacked stages (translation stage, tilt stage, spindle, positioning hexapod) that enable a wide range of experimental configurations. The resulting mechanical structure exhibits complex dynamics with multiple resonance modes in the low frequency range. This dynamic complexity poses significant challenges for the design and control of the active platform.

The primary control requirements focus on $[D_y, D_z, R_y]$ motions; however, the continuous rotation of the active platform requires the control of $[D_x, D_y, D_z, R_x, R_y]$ in the active platform's reference frame.

1.2 Active Vibration Platform

The choice of the active platform architecture for the NASS requires careful consideration of several critical specifications. The platform must provide control over five degrees of freedom ($D_x, D_y, D_z, R_x,$ and R_y), with strokes exceeding $100\ \mu\text{m}$ to correct for micro-station positioning errors, while fitting within a cylindrical envelope of 300 mm diameter and 95 mm height. It must accommodate payloads up to 50 kg while maintaining high dynamical performance. For light samples, the typical design strategy of maximizing actuator stiffness works well because resonance frequencies in the kilohertz range can be achieved, enabling control bandwidths up to 100 Hz. However, achieving such resonance frequencies with a 50 kg payload would require unrealistic stiffness values of approximately $2000\ \text{N}/\mu\text{m}$. This limitation necessitates alternative control approaches, and the High Authority Control/Low Authority Control (HAC-LAC) strategy is proposed to address this challenge. To this purpose, the design includes force sensors for active damping. Compliant mechanisms must also be used to eliminate friction and backlash, which would otherwise compromise the nano-positioning capabilities.

Two primary categories of positioning platform architectures are considered: serial and parallel mechanisms. Serial robots, characterized by open-loop kinematic chains, typically dedicate one actuator per degree of freedom as shown in Figure 1.3a. While offering large workspaces and high maneuverability, serial mechanisms suffer from several inherent limitations. These include low structural stiffness, cumulative positioning errors along the kinematic chain, high mass-to-payload ratios due to actuator placement, and limited payload capacity [14]. These limitations generally make serial architectures unsuitable for nano-positioning applications, except when handling very light samples, as was used in [1] and shown in Figure 1.1a.

In contrast, parallel mechanisms, which connect the mobile platform to the fixed base through multiple parallel struts, offer several advantages for precision positioning. Their closed-loop kinematic structure provides inherently higher structural stiffness, as the platform is simultaneously supported by multiple struts [14]. Although parallel mechanisms typically exhibit limited workspace compared to serial architectures, this limitation is not critical for NASS given its modest stroke requirements. Numerous parallel kinematic architectures have been developed [15] to address various positioning requirements, with designs varying based on the desired degrees of freedom and specific application constraints. Furthermore, hybrid architectures combining both serial and parallel elements have been proposed [16], as illustrated in Figure 1.3, offering potential compromises between the advantages of both approaches.

After evaluating the different options, the Stewart platform architecture was selected for several reasons. In addition to providing control over all required degrees of freedom, its compact design and predictable dynamic characteristics make it particularly suitable for nano-positioning when combined with flexible joints. Stewart platforms have been implemented in a wide variety of configurations, as illustrated in Figure 1.4, which shows two distinct implementations: one utilizing piezoelectric actuators for nano-positioning applications, and another based on voice coil actuators for vibration isolation.

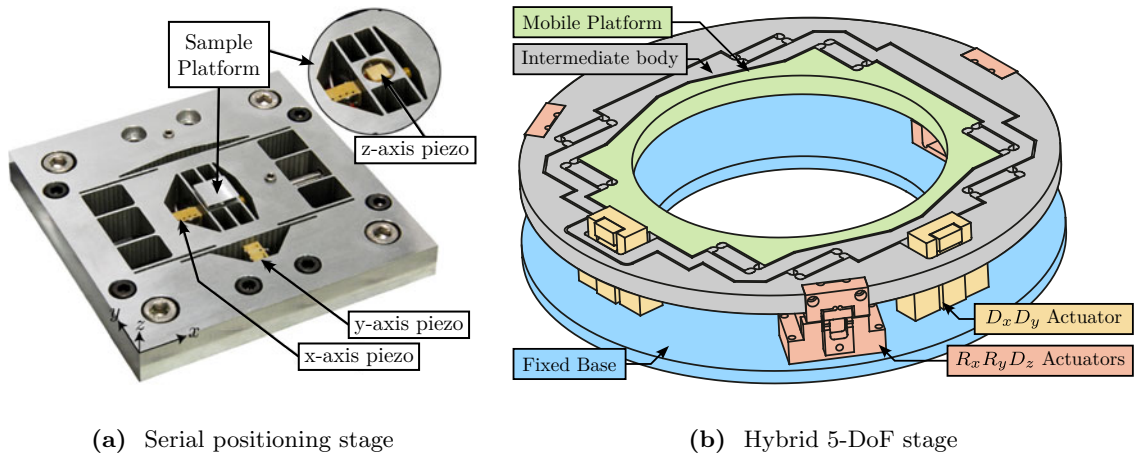
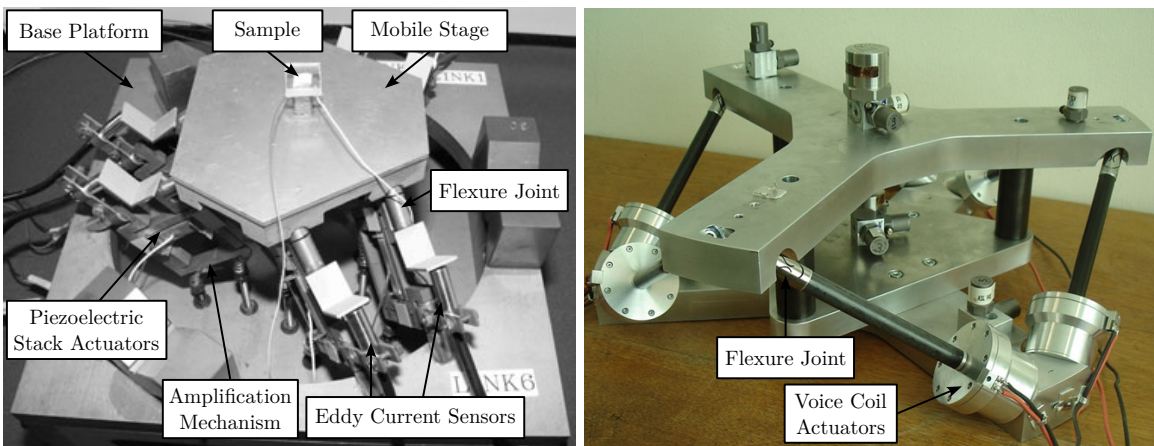


Figure 1.3: Examples of an XYZ serial positioning stage [17] (a) and of a 5-DoF hybrid (parallel/serial) positioning platform [16] (b).

These examples demonstrate the architecture’s versatility in terms of geometry, actuator selection, and scale, all of which can be optimized for specific applications. Furthermore, the successful implementation of Integral Force Feedback (IFF) control on Stewart platforms has been well documented [18], [19], [20], and the extensive body of research on this architecture enables thorough optimization specifically for the NASS.



(a) Stewart platform for Nano-positioning (b) Stewart platform for vibration isolation

Figure 1.4: Two examples of Stewart platform. A Stewart platform based on piezoelectric stack actuators and used for nano-positioning is shown in (a) [21]. A Stewart platform based on voice coil actuators and used for vibration isolation is shown in (b) [20], [22]

2 The Stewart platform

The Stewart platform, first introduced by Stewart in 1965 [23] for flight simulation applications, represents a significant milestone in parallel manipulator design. This mechanical architecture has evolved far beyond its original purpose, and has been applied across diverse field, from precision positioning systems to robotic surgery. The fundamental design consists of two platforms connected by six adjustable struts in parallel, creating a fully parallel manipulator capable of six degrees of freedom motion.

Unlike serial manipulators, in which errors worsen through the kinematic chain, parallel architectures distribute loads across multiple actuators, leading to enhanced mechanical stiffness and improved positioning accuracy. This parallel configuration also results in superior dynamic performance because the actuators directly contribute to the platform’s motion without intermediate linkages. These characteristics make the Stewart platforms particularly valuable in applications requiring high precision and stiffness.

For the NASS application, the Stewart platform architecture offers three key advantages. First, as a fully parallel manipulator, all the motion errors of the micro-station can be compensated through the coordinated action of the six actuators. Second, its compact design compared to serial manipulators makes it ideal for integration on top micro-station where only 95 mm of height is available. Third, the good dynamical properties should enable high-bandwidth positioning control.

While Stewart platforms excel in precision and stiffness, they typically exhibit a relatively limited workspace compared to serial manipulators. However, this limitation is not significant for the NASS application, as the required motion range corresponds to the positioning errors of the micro-station, which are in the order of $10\ \mu\text{m}$.

This section provides a comprehensive analysis of the Stewart platform’s properties, focusing on aspects crucial for precision positioning applications. The analysis encompasses the platform’s kinematic relationships (Section 2.2), the use of the Jacobian matrix (Section 2.3), static behavior (Section 2.4), and dynamic characteristics (Section 2.5). These theoretical foundations form the basis for subsequent design decisions and control strategies, which will be elaborated in later sections.

2.1 Mechanical Architecture

The Stewart platform consists of two rigid platforms connected by six parallel struts (Figure 2.1). Each strut is modelled with an active prismatic joint that allows for controlled length variation, with its ends attached to the fixed and mobile platforms through joints. The typical configuration consists of a universal joint at one end and a spherical joint at the other, providing the necessary degrees of freedom¹.

To facilitate the rigorous analysis of the Stewart platform, four reference frames were defined:

¹Different architecture exists, typically referred as “6-SPS” (Spherical, Prismatic, Spherical) or “6-UPS” (Universal, Prismatic, Spherical)

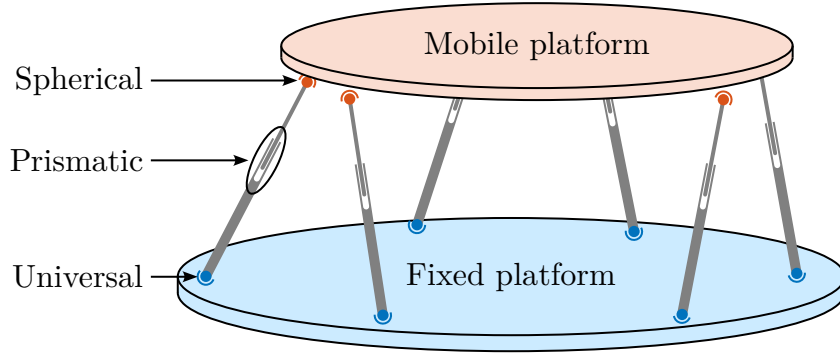


Figure 2.1: Schematical representation of the Stewart platform architecture.

- The fixed base frame $\{F\}$, which is located at the center of the base platform's bottom surface, serves as the mounting reference for the support structure.
- The mobile frame $\{M\}$, which is located at the center of the top platform's upper platform, provides a reference for payload mounting.
- The point-of-interest frame $\{A\}$, fixed to the base but positioned at the workspace center.
- The moving point-of-interest frame $\{B\}$, attached to the mobile platform coincides with frame $\{A\}$ in the home position.

Frames $\{F\}$ and $\{M\}$ serve primarily to define the joint locations. In contrast, frames $\{A\}$ and $\{B\}$ are used to describe the relative motion of the two platforms through the position vector ${}^A\mathbf{P}_B$ of frame $\{B\}$ expressed in frame $\{A\}$ and the rotation matrix ${}^A\mathbf{R}_B$ expressing the orientation of $\{B\}$ with respect to $\{A\}$. For the nano-hexapod, frames $\{A\}$ and $\{B\}$ are chosen to be located at the theoretical focus point of the X-ray light which is 150 mm above the top platform, i.e. above $\{M\}$.

The location of the joints and the orientation and length of the struts are crucial for subsequent kinematic, static, and dynamic analyses of the Stewart platform. The center of rotation for the joint fixed to the base is noted \mathbf{a}_i , while \mathbf{b}_i is used for the top platform joints. The struts' orientations are represented by the unit vectors $\hat{\mathbf{s}}_i$ and their lengths are represented by the scalars l_i . This is summarized in Figure 2.2.

2.2 Kinematic Analysis

Loop Closure

The foundation of the kinematic analysis lies in the geometric constraints imposed by each strut, which can be expressed using loop closure equations. For each strut i (illustrated in Figure 2.3), the loop closure equation (2.1) can be written.

$${}^A\mathbf{P}_B = {}^A\mathbf{a}_i + l_i {}^A\hat{\mathbf{s}}_i - \underbrace{{}^B\mathbf{b}_i}_{{}^A\mathbf{R}_B {}^B\mathbf{b}_i} \quad \text{for } i = 1 \text{ to } 6 \quad (2.1)$$

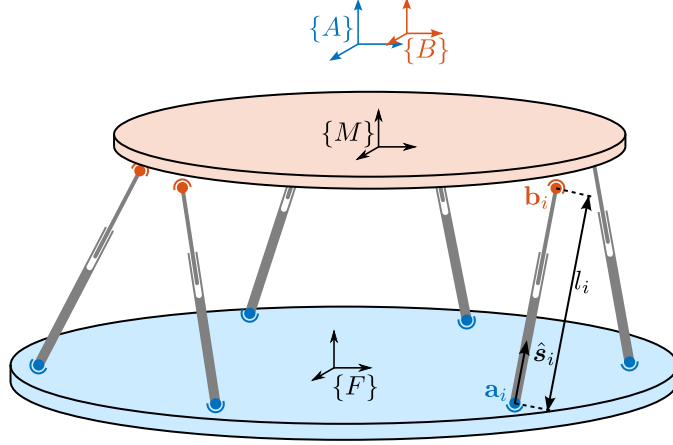


Figure 2.2: Frame and key notations for the Stewart platform

This equation links the pose² variables ${}^A\mathbf{P}$ and ${}^A\mathbf{R}_B$, the position vectors describing the known geometry of the base and the moving platform, \mathbf{a}_i and \mathbf{b}_i , and the strut vector $l_i{}^A\hat{\mathbf{s}}_i$:

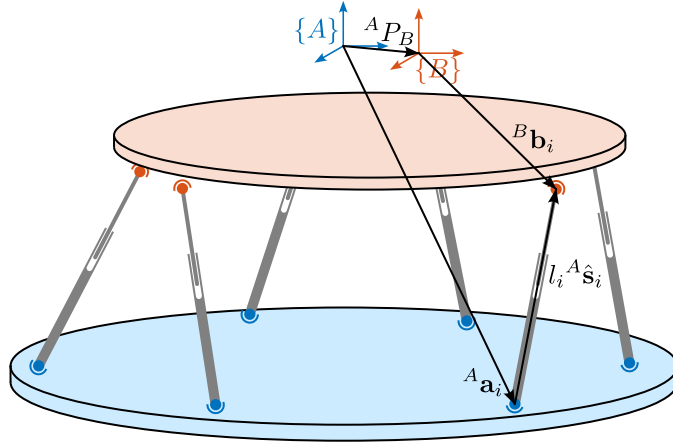


Figure 2.3: Notations to compute the kinematic loop closure

Inverse Kinematics

The inverse kinematic problem involves determining the required strut lengths $\mathcal{L} = [l_1, l_2, \dots, l_6]^\top$ for a desired platform pose \mathcal{X} (i.e. position ${}^A\mathbf{P}$ and orientation ${}^A\mathbf{R}_B$). This problem can be solved analytically using the loop closure equations (2.1). The obtained strut lengths are given by (2.2).

$$l_i = \sqrt{{}^A\mathbf{P}^\top {}^A\mathbf{P} + {}^B\mathbf{b}_i^\top {}^B\mathbf{b}_i + {}^A\mathbf{a}_i^\top {}^A\mathbf{a}_i - 2{}^A\mathbf{P}^\top {}^A\mathbf{a}_i + 2{}^A\mathbf{P}^\top [{}^A\mathbf{R}_B {}^B\mathbf{b}_i] - 2[{}^A\mathbf{R}_B {}^B\mathbf{b}_i]^\top {}^A\mathbf{a}_i} \quad (2.2)$$

If the position and orientation of the platform lie in the feasible workspace, the solution is unique. While configurations outside this workspace yield complex numbers, this only becomes relevant for large displacements that far exceed the nano-hexapod's operating range.

²The *pose* represents the position and orientation of an object

Forward Kinematics

The forward kinematic problem seeks to determine the platform pose \mathcal{X} given a set of strut lengths \mathcal{L} . Unlike inverse kinematics, this presents a significant challenge because it requires solving a system of nonlinear equations. Although various numerical methods exist for solving this problem, they can be computationally intensive and may not guarantee convergence to the correct solution.

For the nano-hexapod application, where displacements are typically small, an approximate solution based on linearization around the operating point provides a practical alternative. This approximation, which is developed in subsequent sections through the Jacobian matrix analysis, is particularly useful for real-time control applications.

2.3 The Jacobian Matrix

The Jacobian matrix plays a central role in analyzing the Stewart platform's behavior, providing a linear mapping between the platform and actuator velocities. While the previously derived kinematic relationships are essential for position analysis, the Jacobian enables velocity analysis and forms the foundation for both static and dynamic studies.

Jacobian Computation

As discussed in Section 2.2, the strut lengths \mathcal{L} and the platform pose \mathcal{X} are related through a system of nonlinear algebraic equations representing the kinematic constraints imposed by the struts.

By taking the time derivative of the position loop close (2.1), equation (2.3) is obtained³.

$${}^A\mathbf{v}_p + {}^A\dot{\mathbf{R}}_B {}^B\mathbf{b}_i + \underbrace{{}^A\mathbf{R}_B {}^B\dot{\mathbf{b}}_i}_{=0} = \dot{l}_i {}^A\hat{\mathbf{s}}_i + l_i \underbrace{{}^A\dot{\hat{\mathbf{s}}}_i}_{=0} + \underbrace{{}^A\dot{\mathbf{a}}_i}_{=0} \quad (2.3)$$

Moreover, we have:

- ${}^A\dot{\mathbf{R}}_B {}^B\mathbf{b}_i = {}^A\boldsymbol{\omega} \times {}^A\mathbf{R}_B {}^B\mathbf{b}_i = {}^A\boldsymbol{\omega} \times {}^A\mathbf{b}_i$ in which ${}^A\boldsymbol{\omega}$ denotes the angular velocity of the moving platform expressed in the fixed frame $\{\mathbf{A}\}$.
- $l_i {}^A\dot{\hat{\mathbf{s}}}_i = l_i ({}^A\boldsymbol{\omega}_i \times \hat{\mathbf{s}}_i)$ in which ${}^A\boldsymbol{\omega}_i$ is the angular velocity of strut i express in fixed frame $\{\mathbf{A}\}$.

By multiplying both sides by ${}^A\hat{\mathbf{s}}_i$, (2.4) is obtained.

$${}^A\hat{\mathbf{s}}_i {}^A\mathbf{v}_p + \underbrace{{}^A\hat{\mathbf{s}}_i ({}^A\boldsymbol{\omega} \times {}^A\mathbf{b}_i)}_{=({}^A\mathbf{b}_i \times {}^A\hat{\mathbf{s}}_i) {}^A\boldsymbol{\omega}} = \dot{l}_i + \underbrace{{}^A\hat{\mathbf{s}}_i l_i ({}^A\boldsymbol{\omega}_i \times \hat{\mathbf{s}}_i)}_{=0} \quad (2.4)$$

Equation (2.4) can be rearranged in matrix form to obtain (2.5), with $\dot{\mathcal{L}} = [\dot{l}_1 \dots \dot{l}_6]^\top$ the vector of strut velocities, and $\dot{\mathcal{X}} = [{}^A\mathbf{v}_p, {}^A\boldsymbol{\omega}]^\top$ the vector of platform velocity and angular velocity.

³Such equation is called the *velocity loop closure*

$$\dot{\mathcal{L}} = \mathbf{J}\dot{\mathcal{X}} \quad (2.5)$$

The matrix \mathbf{J} is called the Jacobian matrix and is defined by (2.6), with ${}^A\hat{\mathbf{s}}_i$ the orientation of the struts expressed in $\{A\}$ and ${}^A\mathbf{b}_i$ the position of the joints with respect to O_B and express in $\{A\}$.

$$\mathbf{J} = \begin{bmatrix} {}^A\hat{\mathbf{s}}_1^\top & ({}^A\mathbf{b}_1 \times {}^A\hat{\mathbf{s}}_1)^\top \\ {}^A\hat{\mathbf{s}}_2^\top & ({}^A\mathbf{b}_2 \times {}^A\hat{\mathbf{s}}_2)^\top \\ {}^A\hat{\mathbf{s}}_3^\top & ({}^A\mathbf{b}_3 \times {}^A\hat{\mathbf{s}}_3)^\top \\ {}^A\hat{\mathbf{s}}_4^\top & ({}^A\mathbf{b}_4 \times {}^A\hat{\mathbf{s}}_4)^\top \\ {}^A\hat{\mathbf{s}}_5^\top & ({}^A\mathbf{b}_5 \times {}^A\hat{\mathbf{s}}_5)^\top \\ {}^A\hat{\mathbf{s}}_6^\top & ({}^A\mathbf{b}_6 \times {}^A\hat{\mathbf{s}}_6)^\top \end{bmatrix} \quad (2.6)$$

Therefore, the Jacobian matrix \mathbf{J} links the rate of change of the strut length to the velocity and angular velocity of the top platform with respect to the fixed base through a set of linear equations. However, \mathbf{J} needs to be recomputed for every Stewart platform pose because it depends on the actual pose of the manipulator.

Approximate solution to the Forward and Inverse Kinematic problems

For small displacements $\delta\mathcal{X} = [\delta x, \delta y, \delta z, \delta\theta_x, \delta\theta_y, \delta\theta_z]^\top$ around an operating point \mathcal{X}_0 (for which the Jacobian was computed), the associated joint displacement $\delta\mathcal{L} = [\delta l_1, \delta l_2, \delta l_3, \delta l_4, \delta l_5, \delta l_6]^\top$ can be computed using the Jacobian (2.7).

$$\delta\mathcal{L} = \mathbf{J}\delta\mathcal{X} \quad (2.7)$$

Similarly, for small joint displacements $\delta\mathcal{L}$, it is possible to find the induced small displacement of the mobile platform (2.8).

$$\delta\mathcal{X} = \mathbf{J}^{-1}\delta\mathcal{L} \quad (2.8)$$

These two relations solve the forward and inverse kinematic problems for small displacement in a *approximate* way. While this approximation offers limited value for inverse kinematics, which can be solved analytically, it proves particularly useful for the forward kinematic problem where exact analytical solutions are difficult to obtain.

Range validity of the approximate inverse kinematics

The accuracy of the Jacobian-based forward kinematics solution was estimated by a simple analysis. For a series of platform positions, the exact strut lengths are computed using the analytical inverse kinematics equation (2.2). These strut lengths are then used with the Jacobian to estimate the platform pose (2.8), from which the error between the estimated and true poses can be calculated, both in terms of position ϵ_D and orientation ϵ_R .

For motion strokes from $1\ \mu\text{m}$ to $10\ \text{mm}$, the errors are estimated for all direction of motion, and the worst case errors are shown in Figure 2.4. The results demonstrate that for displacements up to approximately 1% of the hexapod's size (which corresponds to $100\ \mu\text{m}$ as the size of the Stewart platform is here $\approx 100\ \text{mm}$), the Jacobian approximation provides excellent accuracy.

Since the maximum required stroke of the nano-hexapod ($\approx 100\ \mu\text{m}$) is three orders of magnitude smaller than its overall size ($\approx 100\ \text{mm}$), the Jacobian matrix can be considered constant throughout the workspace. It can be computed once at the rest position and used for both forward and inverse kinematics with high accuracy.

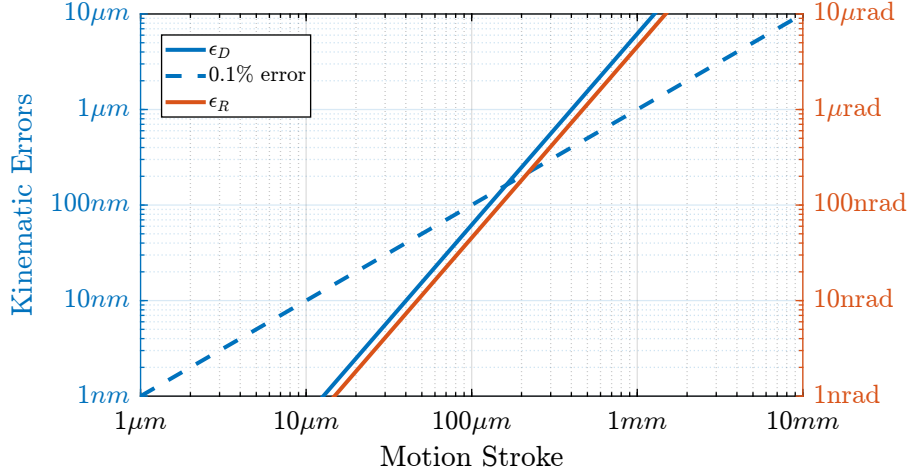


Figure 2.4: Errors associated with the use of the Jacobian matrix to solve the forward kinematic problem. A Stewart platform with a height of $100\ \text{mm}$ was used to perform this analysis. ϵ_D corresponds to the distance between the true position and the estimated position. ϵ_R corresponds to the angular motion between the true orientation and the estimated orientation.

Static Forces

The static force analysis of the Stewart platform can be performed using the principle of virtual work. This principle states that for a system in static equilibrium, the total virtual work of all forces acting on the system must be zero for any virtual displacement compatible with the system's constraints.

Let $\mathbf{f} = [f_1, f_2, \dots, f_6]^\top$ represent the vector of actuator forces applied in each strut, and $\mathcal{F} = [\mathbf{F}, \mathbf{n}]^\top$ denote the external wrench (combined force \mathbf{F} and torque \mathbf{n}) acting on the mobile platform at point \mathcal{O}_B . The virtual work δW consists of two contributions:

- The work performed by the actuator forces through virtual strut displacements $\delta\mathcal{L}$: $\mathbf{f}^\top \delta\mathcal{L}$
- The work performed by the external wrench through virtual platform displacements $\delta\mathcal{X}$: $-\mathcal{F}^\top \delta\mathcal{X}$

Thus, the principle of virtual work can be expressed as:

$$\delta W = \mathbf{f}^\top \delta\mathcal{L} - \mathcal{F}^\top \delta\mathcal{X} = 0 \quad (2.9)$$

Using the Jacobian relationship that links virtual displacements (2.7), this equation becomes:

$$(\mathbf{f}^\top \mathbf{J} - \mathcal{F}^\top) \delta \mathcal{X} = 0 \quad (2.10)$$

Because this equation must hold for any virtual displacement $\delta \mathcal{X}$, the force mapping relationships (2.11) can be derived.

$$\mathbf{f}^\top \mathbf{J} - \mathcal{F}^\top = 0 \quad \Rightarrow \quad \boxed{\mathcal{F} = \mathbf{J}^\top \mathbf{f}} \quad \text{and} \quad \boxed{\mathbf{f} = \mathbf{J}^{-T} \mathcal{F}} \quad (2.11)$$

These equations establish that the transpose of the Jacobian matrix maps actuator forces to platform forces and torques, while its inverse transpose maps platform forces and torques to required actuator forces.

2.4 Static Analysis

The static stiffness characteristics of the Stewart platform play a crucial role in its performance, particularly for precision positioning applications. These characteristics are fundamentally determined by both the actuator properties and the platform geometry.

Starting from the individual actuators, the relationship between applied force f_i and resulting displacement δl_i for each strut i is characterized by its stiffness k_i :

$$f_i = k_i \delta l_i, \quad i = 1, \dots, 6 \quad (2.12)$$

These individual relationships can be combined into a matrix form using the diagonal stiffness matrix \mathcal{K} :

$$\mathbf{f} = \mathcal{K} \cdot \delta \mathcal{L}, \quad \mathcal{K} = \text{diag}[k_1, \dots, k_6] \quad (2.13)$$

By applying the force mapping relationships (2.11) derived in the previous section and the Jacobian relationship for small displacements (2.8), the relationship between applied wrench \mathcal{F} and resulting platform displacement $\delta \mathcal{X}$ is obtained (2.14).

$$\mathcal{F} = \underbrace{\mathbf{J}^\top \mathcal{K} \mathbf{J}}_{\mathbf{K}} \cdot \delta \mathcal{X} \quad (2.14)$$

where $\mathbf{K} = \mathbf{J}^\top \mathcal{K} \mathbf{J}$ is identified as the platform stiffness matrix.

The inverse relationship is given by the compliance matrix \mathbf{C} :

$$\delta \mathcal{X} = \underbrace{(\mathbf{J}^\top \mathcal{K} \mathbf{J})^{-1}}_{\mathbf{C}} \mathcal{F} \quad (2.15)$$

These relationships reveal that the overall platform stiffness and compliance characteristics are determined by two factors:

- The individual actuator stiffnesses represented by \mathcal{K}
- The geometric configuration embodied in the Jacobian matrix \mathbf{J}

This geometric dependency means that the platform's stiffness varies throughout its workspace, as the Jacobian matrix changes with the platform's position and orientation. For the NASS application, where the workspace is small compared to the platform dimensions, these variations can be considered negligible. However, the initial geometric configuration significantly affects the overall stiffness characteristics. The relationship between maximum stroke and stiffness presents another important design consideration. As both parameters are influenced by the geometric configuration, their optimization involves inherent trade-offs that must be carefully balanced based on the application requirements. The optimization of this configuration to achieve the desired stiffness while having sufficient stroke will be addressed during the detailed design phase.

2.5 Dynamical Analysis

For initial analysis, a simplified representation of the system has been developed. This model assumes perfectly rigid bodies for both the platform and base, connected by massless struts through ideal joints that exhibit neither friction nor compliance.

Under these assumptions, the system dynamics can be expressed in Cartesian space as:

$$\mathbf{M}s^2\mathcal{X} = \Sigma\mathcal{F} \quad (2.16)$$

where \mathbf{M} represents the platform mass matrix, \mathcal{X} the platform pose, and $\Sigma\mathcal{F}$ the sum of forces acting on the platform.

The primary forces acting on the system are actuator forces \mathbf{f} , elastic forces due to strut stiffness $-\mathcal{K}\mathcal{L}$ and damping forces in the struts $\mathcal{C}\dot{\mathcal{L}}$.

$$\Sigma\mathcal{F} = \mathbf{J}^T(\mathbf{f} - \mathcal{K}\mathcal{L} - s\mathcal{C}\mathcal{L}), \quad \mathcal{K} = \text{diag}(k_1 \dots k_6), \quad \mathcal{C} = \text{diag}(c_1 \dots c_6) \quad (2.17)$$

Combining these forces and using (2.8) yields the complete dynamic equation (2.18).

$$\mathbf{M}s^2\mathcal{X} = \mathcal{F} - \mathbf{J}^T\mathcal{K}\mathbf{J}\mathcal{X} - \mathbf{J}^T\mathcal{C}\mathbf{J}s\mathcal{X} \quad (2.18)$$

The transfer function matrix in the Cartesian frame becomes (2.19).

$$\frac{\mathcal{X}}{\mathcal{F}}(s) = (\mathbf{M}s^2 + \mathbf{J}^T\mathcal{C}\mathbf{J}s + \mathbf{J}^T\mathcal{K}\mathbf{J})^{-1} \quad (2.19)$$

Through coordinate transformation using the Jacobian matrix, the dynamics in the actuator space is obtained (2.20).

$$\frac{\mathcal{L}}{\mathbf{f}}(s) = (\mathbf{J}^{-T}\mathbf{M}\mathbf{J}^{-1}s^2 + \mathcal{C} + \mathcal{K})^{-1} \quad (2.20)$$

Although this simplified model provides useful insights, real Stewart platforms exhibit more complex behaviors. Several factors can significantly increase the model complexity, such as:

- Strut dynamics, including mass distribution and internal resonances [24], [25]
- Joint compliance and friction effects [26], [27]
- Supporting structure dynamics and payload dynamics, which are both very critical for NASS

These additional effects render analytical modeling impractical for complete system analysis.

Conclusion

The fundamental characteristics of the Stewart platform have been analyzed in this chapter. Essential kinematic relationships were developed through loop closure equations, from which both exact and approximate solutions for the inverse and forward kinematic problems were derived. The Jacobian matrix was established as a central mathematical tool through which crucial insights into velocity relationships, static force transmission, and dynamic behavior of the platform were obtained.

For the NASS application, where displacements are typically limited to the micrometer range, the accuracy of linearized models using a constant Jacobian matrix has been demonstrated, by which both analysis and control can be significantly simplified. However, additional complexities such as strut masses, joint compliance, and supporting structure dynamics must be considered in the full dynamic behavior. This will be performed in the next section using a multi-body model.

All these characteristics (maneuverability, stiffness, dynamics, etc.) are fundamentally determined by the platform's geometry. While a reasonable geometric configuration will be used to validate the NASS during the conceptual phase, the optimization of these geometric parameters will be explored during the detailed design phase.

3 Multi-Body Model

The dynamic modeling of Stewart platforms has traditionally relied on analytical approaches. However, these analytical models become increasingly complex when the dynamical behaviors of struts and joints must be captured. To overcome these limitations, a flexible multi-body approach was developed that can be readily integrated into the broader NASS model. Through this multi-body modeling approach, each component model (including joints, actuators, and sensors) can be progressively refined.

The analysis is structured as follows. First, the multi-body model is developed, and the geometric parameters, inertial properties, and actuator characteristics are established (Section 3.1). The model is then validated through comparison with the analytical equations in a simplified configuration (Section 3.2). Finally, the validated model is employed to analyze the nano-hexapod dynamics, from which insights for the control system design are derived (Section 3.3).

3.1 Model Definition

Geometry

The Stewart platform's geometry is defined by two principal coordinate frames (Figure 3.1): a fixed base frame $\{F\}$ and a moving platform frame $\{M\}$. The joints connecting the actuators to these frames are located at positions ${}^F\mathbf{a}_i$ and ${}^M\mathbf{b}_i$ respectively. The point of interest, denoted by frame $\{A\}$, is situated 150 mm above the moving platform frame $\{M\}$.

The geometric parameters of the nano-hexapod are summarized in Table 3.1. These parameters define the positions of all connection points in their respective coordinate frames. From these parameters, key kinematic properties can be derived: the strut orientations $\hat{\mathbf{s}}_i$, strut lengths l_i , and the system's Jacobian matrix \mathbf{J} .

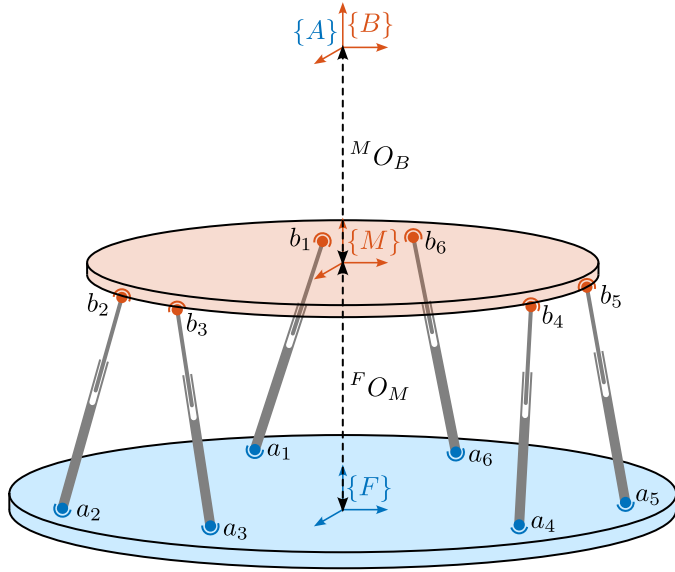


Figure 3.1: Geometry of the Stewart platform

| | x | y | z |
|---------------------|------|------|-----|
| ${}^M O_B$ | 0 | 0 | 150 |
| ${}^F O_M$ | 0 | 0 | 95 |
| ${}^F \mathbf{a}_1$ | -92 | -77 | 20 |
| ${}^F \mathbf{a}_2$ | 92 | -77 | 20 |
| ${}^F \mathbf{a}_3$ | 113 | -41 | 20 |
| ${}^F \mathbf{a}_4$ | 21 | 118 | 20 |
| ${}^F \mathbf{a}_5$ | -21 | 118 | 20 |
| ${}^F \mathbf{a}_6$ | -113 | -41 | 20 |
| ${}^M \mathbf{b}_1$ | -28 | -106 | -20 |
| ${}^M \mathbf{b}_2$ | 28 | -106 | -20 |
| ${}^M \mathbf{b}_3$ | 106 | 28 | -20 |
| ${}^M \mathbf{b}_4$ | 78 | 78 | -20 |
| ${}^M \mathbf{b}_5$ | -78 | 78 | -20 |
| ${}^M \mathbf{b}_6$ | -106 | 28 | -20 |

Table 3.1: Parameter values in [mm]

Inertia of Plates

The fixed base and moving platform were modeled as solid cylindrical bodies. The base platform was characterized by a radius of 120 mm and thickness of 15 mm , matching the dimensions of the microhexapod's top platform. The moving platform was similarly modeled with a radius of 110 mm and thickness of 15 mm . Both platforms were assigned a mass of 5 kg .

Joints

The platform's joints play a crucial role in its dynamic behavior. At both the upper and lower connection points, various degrees of freedom can be modeled, including universal joints, spherical joints, and configurations with additional axial and lateral stiffness components. For each degree of freedom, stiffness characteristics can be incorporated into the model.

In the conceptual design phase, a simplified joint configuration is employed: the bottom joints are modeled as two-degree-of-freedom universal joints, while the top joints are represented as three-degree-of-freedom spherical joints. These joints are considered massless and exhibit no stiffness along their degrees of freedom.

Actuators

The actuator model comprises several key elements (Figure 3.2). At its core, each actuator is modeled as a prismatic joint with internal stiffness k_a and damping c_a , driven by a force source f . Similarly to what was found using the rotating 3-DoF model, a parallel stiffness k_p is added in parallel with the force sensor to ensure stability when considering spindle rotation effects.

Each actuator is equipped with two sensors: a force sensor providing measurements f_n and a relative motion sensor that measures the strut length l_i . The actuator parameters used in the conceptual phase are listed in Table 3.2.

This modular approach to actuator modeling allows for future refinements as the design evolves, enabling the incorporation of additional dynamic effects or sensor characteristics as needed.

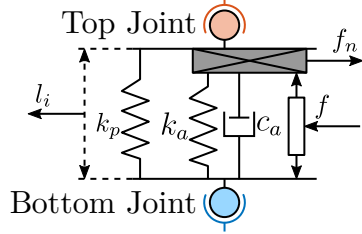


Figure 3.2: Model of the nano-hexapod actuators

| | Value |
|-------|------------------------------------|
| k_a | $1 \text{ N}/\mu\text{m}$ |
| c_a | $50 \text{ N}/(\text{m}/\text{s})$ |
| k_p | $0.05 \text{ N}/\mu\text{m}$ |

Table 3.2: Actuator parameters

3.2 Validation of the multi-body model

The developed multi-body model of the Stewart platform is represented schematically in Figure 3.3, highlighting the key inputs and outputs: actuator forces \mathbf{f} , force sensor measurements \mathbf{f}_n , and relative displacement measurements \mathcal{L} . The frames $\{F\}$ and $\{M\}$ serve as interfaces for integration with other elements in the multi-body system. A three-dimensional visualization of the model is presented in Figure 3.4.

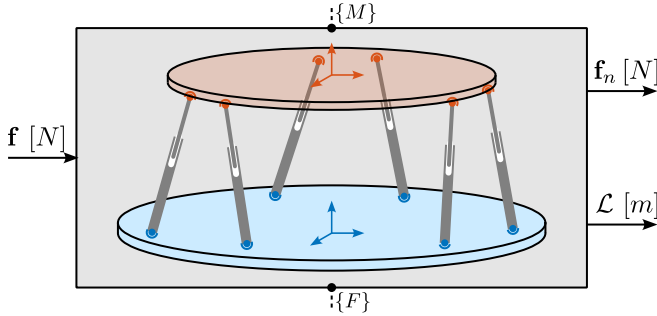


Figure 3.3: Nano-Hexapod plant with inputs and outputs. Frames $\{F\}$ and $\{M\}$ can be connected to other elements in the multi-body models.

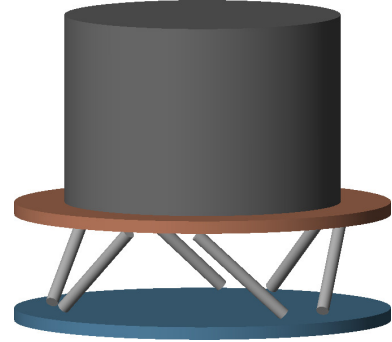


Figure 3.4: 3D representation of the multi-body model

The validation of the multi-body model was performed using the simplest Stewart platform configuration, enabling direct comparison with the analytical transfer functions derived in Section 2.5. This configuration consists of massless universal joints at the base, massless spherical joints at the top platform, and massless struts with stiffness $k_a = 1 \text{ N}/\mu\text{m}$ and damping $c_a = 10 \text{ N}/(\text{m}/\text{s})$. The geometric parameters remain as specified in Table 3.2.

While the moving platform itself is considered massless, a 10 kg cylindrical payload is mounted on top with a radius of $r = 110 \text{ mm}$ and a height $h = 300 \text{ mm}$.

For the analytical model, the stiffness, damping, and mass matrices are defined in (3.1).

$$\mathcal{K} = \text{diag}(k_a, k_a, k_a, k_a, k_a, k_a) \quad (3.1a)$$

$$\mathcal{C} = \text{diag}(c_a, c_a, c_a, c_a, c_a, c_a) \quad (3.1b)$$

$$\mathbf{M} = \text{diag}\left(m, m, m, \frac{1}{12}m(3r^2 + h^2), \frac{1}{12}m(3r^2 + h^2), \frac{1}{2}mr^2\right) \quad (3.1c)$$

The transfer functions from the actuator forces to the strut displacements are computed using these matrices according to equation (2.20). These analytical transfer functions are then compared with those extracted from the multi-body model. The developed multi-body model yields a state-space representation with 12 states, corresponding to the six degrees of freedom of the moving platform.

Figure 3.5 presents a comparison between the analytical and multi-body transfer functions, specifically showing the response from the first actuator force to all six strut displacements. The close agreement between both approaches across the frequency spectrum validates the multi-body model's accuracy in capturing the system's dynamic behavior.

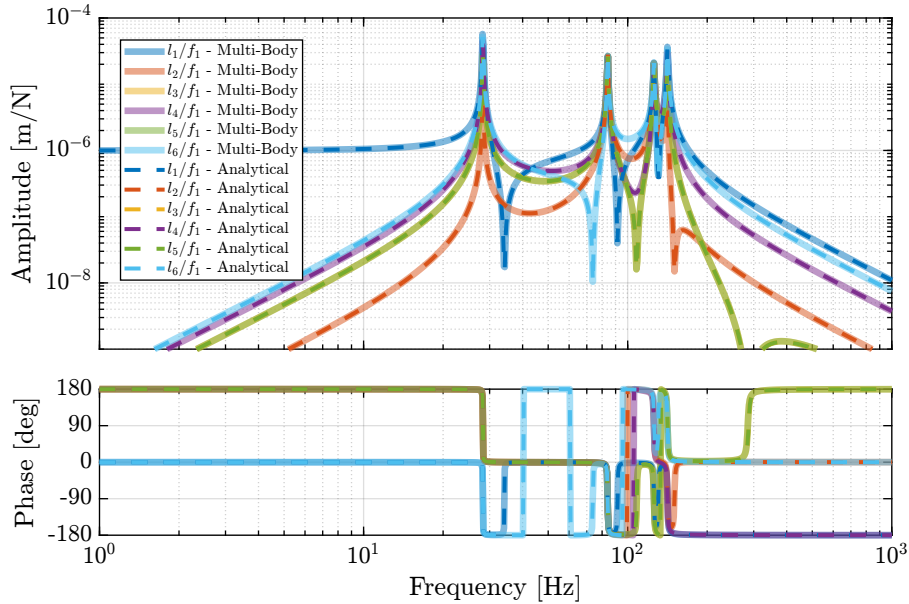


Figure 3.5: Comparison of the analytical transfer functions and the multi-body model

3.3 Nano Hexapod Dynamics

Following the validation of the multi-body model, a detailed analysis of the nano-hexapod dynamics was performed. The model parameters were set according to the specifications outlined in Section 3.1, with a payload mass of 10 kg. The transfer functions from actuator forces \mathbf{f} to both strut displacements \mathcal{L} and force measurements \mathbf{f}_n were derived from the multi-body model.

The transfer functions relating actuator forces to strut displacements are presented in Figure 3.6a. Due to the system's symmetrical design and identical strut configurations, all diagonal terms (transfer functions from force f_i to displacement l_i of the same strut) exhibit identical behavior. While the system has six degrees of freedom, only four distinct resonance frequencies were observed in the frequency

response. This reduction from six to four observable modes is attributed to the system's symmetry, where two pairs of resonances occur at identical frequencies.

The system's behavior can be characterized in three frequency regions. At low frequencies, well below the first resonance, the plant demonstrates good decoupling between actuators, with the response dominated by the strut stiffness: $\mathbf{G}(j\omega) \xrightarrow{\omega \rightarrow 0} \mathbf{K}^{-1}$. In the mid-frequency range, the system exhibits coupled dynamics through its resonant modes, reflecting the complex interactions between the platform's degrees of freedom. At high frequencies, above the highest resonance, the response is governed by the payload's inertia mapped to the strut coordinates: $\mathbf{G}(j\omega) \xrightarrow{\omega \rightarrow \infty} \mathbf{J}\mathbf{M}^{-T}\mathbf{J}^T \frac{1}{\omega^2}$

The force sensor transfer functions, shown in Figure 3.6b, display characteristics typical of collocated actuator-sensor pairs. Each actuator's transfer function to its associated force sensor exhibits alternating complex conjugate poles and zeros. The inclusion of parallel stiffness introduces an additional complex conjugate zero at low frequency, which was previously observed in the three-degree-of-freedom rotating model.

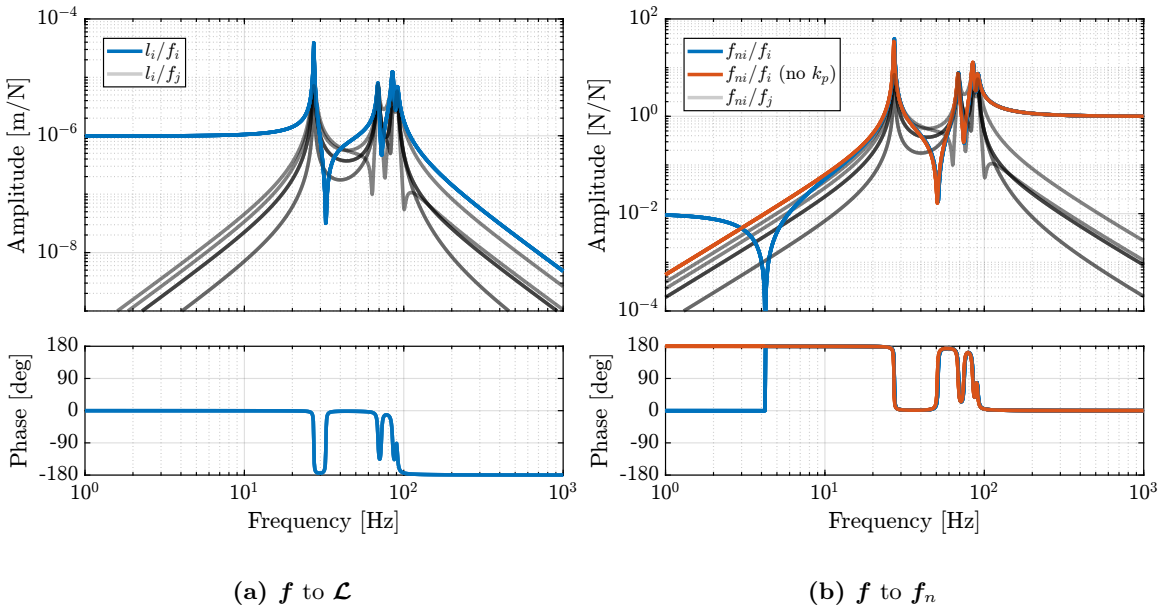


Figure 3.6: Bode plot of the transfer functions computed from the nano-hexapod multi-body model

Conclusion

The multi-body modeling approach presented in this section provides a comprehensive framework for analyzing the dynamics of the nano-hexapod system. Through comparison with analytical solutions in a simplified configuration, the model's accuracy has been validated, demonstrating its ability to capture the essential dynamic behavior of the Stewart platform.

A key advantage of this modeling approach lies in its flexibility for future refinements. While the current implementation employs idealized joints for the conceptual design phase, the framework readily accommodates the incorporation of joint stiffness and other non-ideal effects. The joint stiffness, which is known to impact the performance of decentralized IFF control strategy [20], will be studied and

optimized during the detailed design phase. The validated multi-body model will serve as a valuable tool for predicting system behavior and evaluating control performance throughout the design process.

4 Control of Stewart Platforms

The control of Stewart platforms presents distinct challenges compared to the uniaxial model due to their multi-input multi-output nature. Although the uniaxial model demonstrated the effectiveness of the HAC-LAC strategy, its extension to Stewart platforms requires careful considerations discussed in this section.

First, the distinction between centralized and decentralized control approaches is discussed in Section 4.1. The impact of the control space selection - either Cartesian or strut space - is then analyzed in Section 4.2, highlighting the trade-offs between direction-specific tuning and implementation simplicity.

Building on these analyses, a decentralized active damping strategy using Integral Force Feedback is developed in Section 4.3, followed by the implementation of a centralized High Authority Control for positioning in Section 4.4. This architecture, while simple, will be used to demonstrate the feasibility of the NASS concept and will provide a foundation for more sophisticated control strategies to be developed during the detailed design phase.

4.1 Centralized and Decentralized Control

In the control of MIMO systems, and more specifically of Stewart platforms, a fundamental architectural decision lies in the choice between centralized and decentralized control strategies.

In decentralized control, each actuator operates based on feedback from its associated sensor only, creating independent control loops, as illustrated in Figure 4.1. While mechanical coupling between the struts exists, control decisions are made locally, with each controller processing information from a single sensor-actuator pair. This approach offers simplicity in implementation and reduces computational requirements.

Conversely, centralized control uses information from all sensors to determine the control action of each actuator. This strategy potentially enables better performance by explicitly accounting for the mechanical coupling between the struts, though at the cost of increased complexity in both design and implementation.

The choice between these approaches depends significantly on the degree of interaction between the different control channels, and also on the available sensors and actuators. For instance, when using external metrology systems that measure the platform's global position, centralized control becomes necessary because each sensor measurement depends on all actuator inputs.

In the context of the nano-hexapod, two distinct control strategies were examined during the conceptual phase:

- Decentralized Integral Force Feedback (IFF), which utilizes collocated force sensors to implement independent control loops for each strut (Section 4.3)

- High-Authority Control (HAC), which employs a centralized approach to achieve precise positioning based on external metrology measurements (Section 4.4)

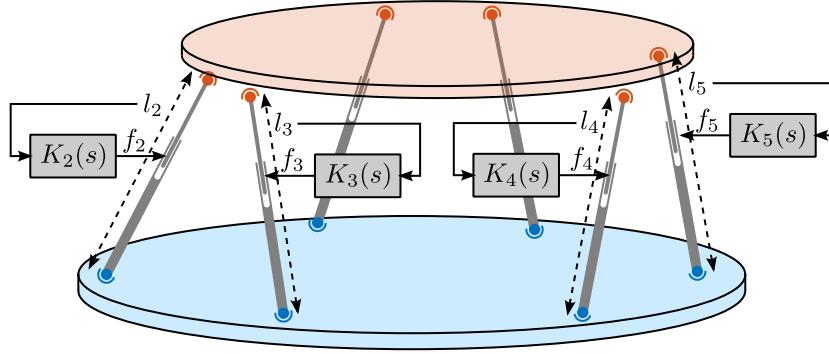


Figure 4.1: Decentralized control strategy using the encoders. The two controllers for the struts on the back are not shown for simplicity.

4.2 Choice of the Control Space

When controlling a Stewart platform using external metrology that measures the pose of frame $\{B\}$ with respect to $\{A\}$, denoted as \mathcal{X} , the control architecture can be implemented in either Cartesian or strut space. This choice affects both the control design and the obtained performance.

Control in the Strut space

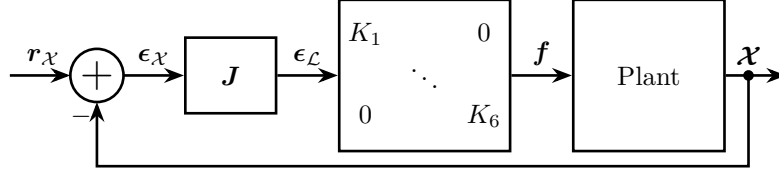
In this approach, as illustrated in Figure 4.2a, the control is performed in the space of the struts. The Jacobian matrix is used to solve the inverse kinematics in real-time by mapping position errors from Cartesian space $\epsilon_{\mathcal{X}}$ to strut space $\epsilon_{\mathcal{L}}$. A diagonal controller then processes these strut-space errors to generate force commands for each actuator.

The main advantage of this approach emerges from the plant characteristics in the strut space, as shown in Figure 4.3a. The diagonal terms of the plant (transfer functions from force to displacement of the same strut, as measured by the external metrology) are identical due to the system's symmetry. This simplifies the control design because only one controller needs to be tuned. Furthermore, at low frequencies, the plant exhibits good decoupling between the struts, allowing for effective independent control of each axis.

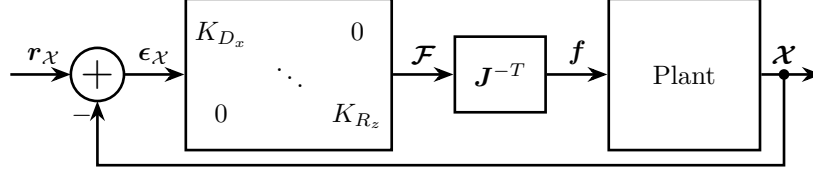
Control in Cartesian Space

Alternatively, control can be implemented directly in Cartesian space, as illustrated in Figure 4.2b. Here, the controller processes Cartesian errors $\epsilon_{\mathcal{X}}$ to generate forces and torques \mathcal{F} , which are then mapped to actuator forces using the transpose of the inverse Jacobian matrix (2.11).

The plant behavior in Cartesian space, illustrated in Figure 4.3b, reveals interesting characteristics. Some degrees of freedom, particularly the vertical translation and rotation about the vertical axis, exhibit simpler second-order dynamics. A key advantage of this approach is that the control performance



(a) Control in the frame of the struts. J is used to project errors in the frame of the struts



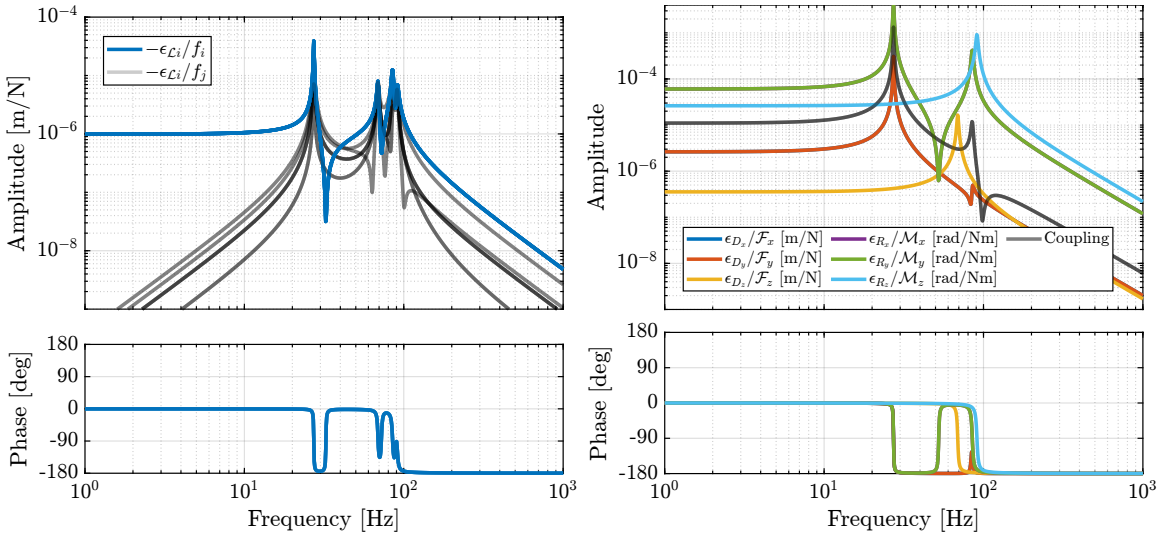
(b) Control in the Cartesian frame. J^{-T} is used to project force and torques on each strut

Figure 4.2: Two control strategies

can be tuned individually for each direction. This is particularly valuable when performance requirements differ between degrees of freedom - for instance, when higher positioning accuracy is required vertically than horizontally, or when certain rotational degrees of freedom can tolerate larger errors than others.

However, significant coupling exists between certain degrees of freedom, particularly between rotations and translations (e.g., $\epsilon_{R_x}/\mathcal{F}_y$ or ϵ_{D_y}/M_x).

For the conceptual validation of the nano-hexapod, control in the strut space was selected due to its simpler implementation and the beneficial decoupling properties observed at low frequencies. More sophisticated control strategies will be explored during the detailed design phase.



(a) Plant in the frame of the struts

(b) Plant in the Cartesian Frame

Figure 4.3: Bode plot of the transfer functions computed from the nano-hexapod multi-body model

4.3 Active Damping with Decentralized IFF

The decentralized Integral Force Feedback (IFF) control strategy is implemented using independent control loops for each strut, similarly to what is shown in Figure 4.1, but using force sensors instead of relative motion sensors.

The corresponding block diagram of the control loop is shown in Figure 4.4, in which the controller $\mathbf{K}_{\text{IFF}}(s)$ is a diagonal matrix, where each diagonal element is a pure integrator (4.1).

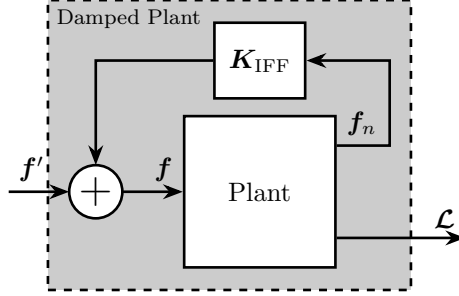


Figure 4.4: Schematic of the implemented decentralized IFF controller. The damped plant has a new inputs \mathbf{f}'

$$\mathbf{K}_{\text{IFF}}(s) = g \cdot \begin{bmatrix} K_{\text{IFF}}(s) & & 0 \\ & \ddots & \\ 0 & & K_{\text{IFF}}(s) \end{bmatrix}, \quad K_{\text{IFF}}(s) = \frac{1}{s} \quad (4.1)$$

In this section, the stiffness in parallel with the force sensor was omitted since the Stewart platform is not subjected to rotation. The effect of this parallel stiffness is examined in the next section when the platform is integrated into the complete NASS.

Root Locus analysis, shown in Figure 4.5b, reveals the evolution of the closed-loop poles as the controller gain g varies from 0 to ∞ . A key characteristic of force feedback control with collocated sensor-actuator pairs is observed: all closed-loop poles are bounded to the left-half plane, indicating guaranteed stability [28]. This property is particularly valuable because the coupling is very large around resonance frequencies, enabling control of modes that would be difficult to include within the bandwidth using position feedback alone.

The bode plot of an individual loop gain (i.e. the loop gain of $K_{\text{IFF}}(s) \cdot \frac{f_{ni}}{f_i}(s)$), presented in Figure 4.5a, exhibits the typical characteristics of integral force feedback of having a phase bounded between -90° and $+90^\circ$. The loop-gain is high around the resonance frequencies, indicating that the decentralized IFF provides significant control authority over these modes. This high gain, combined with the bounded phase, enables effective damping of the resonant modes while maintaining stability.

4.4 MIMO High-Authority Control - Low-Authority Control

The design of the High Authority Control positioning loop is now examined. The complete HAC-IFF control architecture is illustrated in Figure 4.6, where the reference signal $\mathbf{r}_{\mathcal{X}}$ represents the desired pose, and \mathcal{X} is the measured pose by the external metrology system.

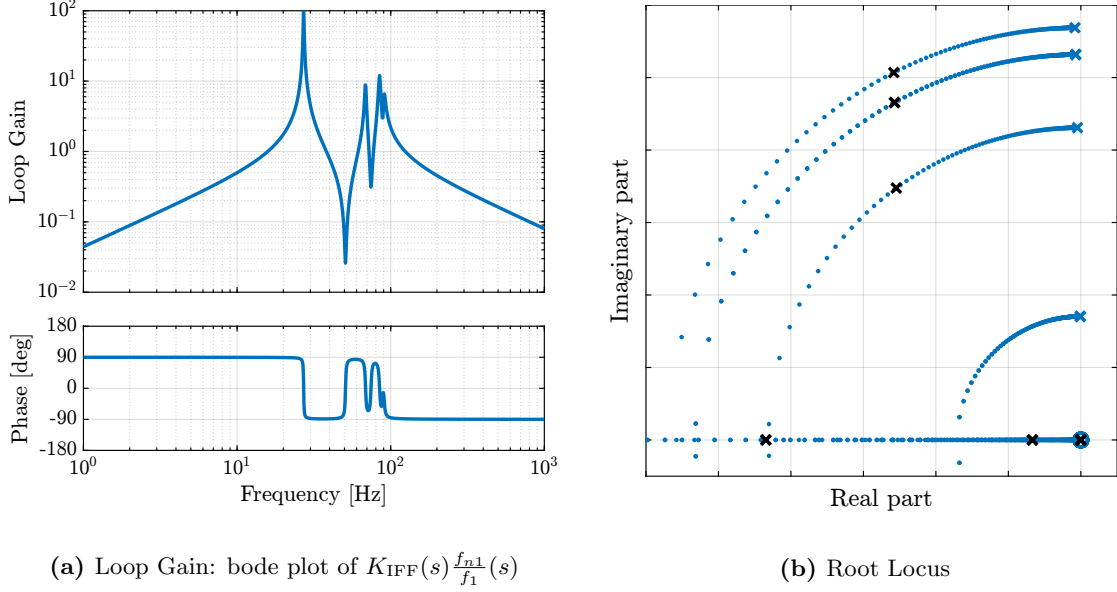


Figure 4.5: Decentralized IFF

Following the analysis from Section 4.2, the control is implemented in the strut space. The Jacobian matrix \mathbf{J}^{-1} performs (approximate) real-time approximate inverse kinematics to map position errors from Cartesian space $\epsilon_{\mathcal{X}}$ to strut space $\epsilon_{\mathcal{L}}$. A diagonal High Authority Controller \mathbf{K}_{HAC} then processes these errors in the frame of the struts.

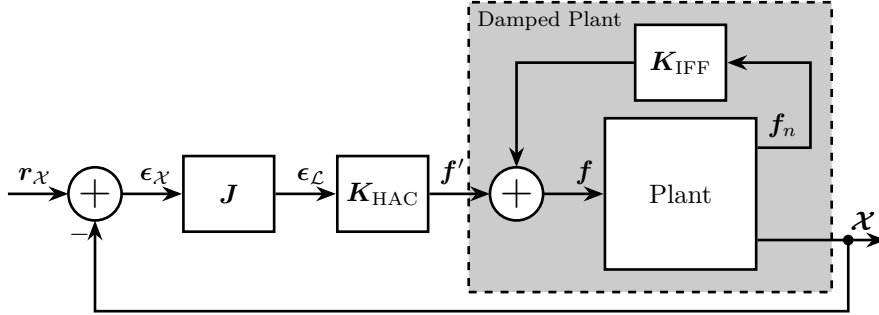
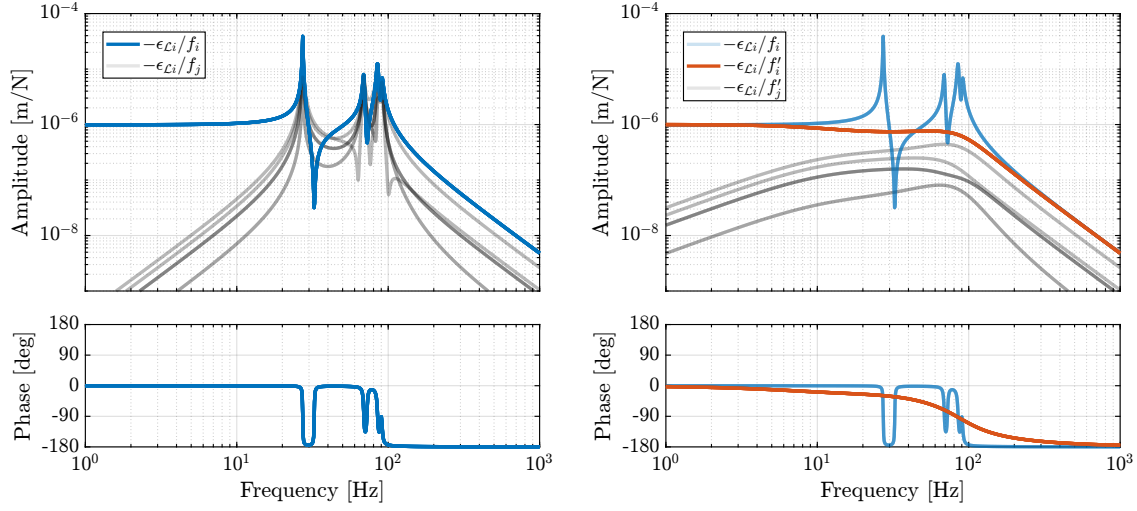


Figure 4.6: HAC-IFF control architecture with the High Authority Controller being implemented in the frame of the struts

The effect of decentralized IFF on the plant dynamics can be observed by comparing two sets of transfer functions. Figure 4.7a shows the original transfer functions from actuator forces \mathbf{f} to strut errors $\epsilon_{\mathcal{L}}$, which are characterized by pronounced resonant peaks. When the decentralized IFF is implemented, the transfer functions from modified inputs \mathbf{f}' to strut errors $\epsilon_{\mathcal{L}}$ exhibit significantly attenuated resonances (Figure 4.7b). This damping of structural resonances serves two purposes: it reduces vibrations near resonances and simplifies the design of the high authority controller by providing simpler plant dynamics.

Based upon the damped plant dynamics shown in Figure 4.7b, a high authority controller was designed with the structure given in (4.2). The controller combines three elements: an integrator providing high gain at low frequencies, a lead compensator improving stability margins, and a low-pass filter for robustness against unmodeled high-frequency dynamics. The loop gain of an individual control channel



(a) Undamped plant in the frame of the struts

(b) Damped plant with Decentralized IFF

Figure 4.7: Plant in the frame of the strut for the High Authority Controller.

is shown in Figure 4.8a.

$$\mathbf{K}_{\text{HAC}}(s) = \begin{bmatrix} K_{\text{HAC}}(s) & & 0 \\ & \ddots & \\ 0 & & K_{\text{HAC}}(s) \end{bmatrix}, \quad K_{\text{HAC}}(s) = g_0 \cdot \underbrace{\frac{\omega_c}{s}}_{\text{int}} \cdot \underbrace{\frac{1}{\sqrt{\alpha}} \frac{1 + \frac{s}{\omega_c/\sqrt{\alpha}}}{1 + \frac{s}{\omega_c\sqrt{\alpha}}}}_{\text{lead}} \cdot \underbrace{\frac{1}{1 + \frac{s}{\omega_0}}}_{\text{LPF}} \quad (4.2)$$

The stability of the MIMO feedback loop is analyzed through the *characteristic loci* method. Such characteristic loci represent the eigenvalues of the loop gain matrix $\mathbf{G}(j\omega)\mathbf{K}(j\omega)$ plotted in the complex plane as the frequency varies from 0 to ∞ . For MIMO systems, this method generalizes the classical Nyquist stability criterion: with the open-loop system being stable, the closed-loop system is stable if none of the characteristic loci encircle the -1 point [29]. As shown in Figure 4.8b, all loci remain to the right of the -1 point, validating the stability of the closed-loop system. Additionally, the distance of the loci from the -1 point provides information about stability margins of the coupled system.

Conclusion

The control architecture developed for the uniaxial and the rotating models was adapted for the Stewart platform.

Two fundamental choices were first addressed: the selection between centralized and decentralized approaches and the choice of control space. While control in Cartesian space enables direction-specific performance tuning, implementation in strut space was selected for the conceptual design phase due to two key advantages: good decoupling at low frequencies and identical diagonal terms in the plant transfer functions, allowing a single controller design to be replicated across all struts.

The HAC-LAC strategy was then implemented. The inner loop implements decentralized Integral Force

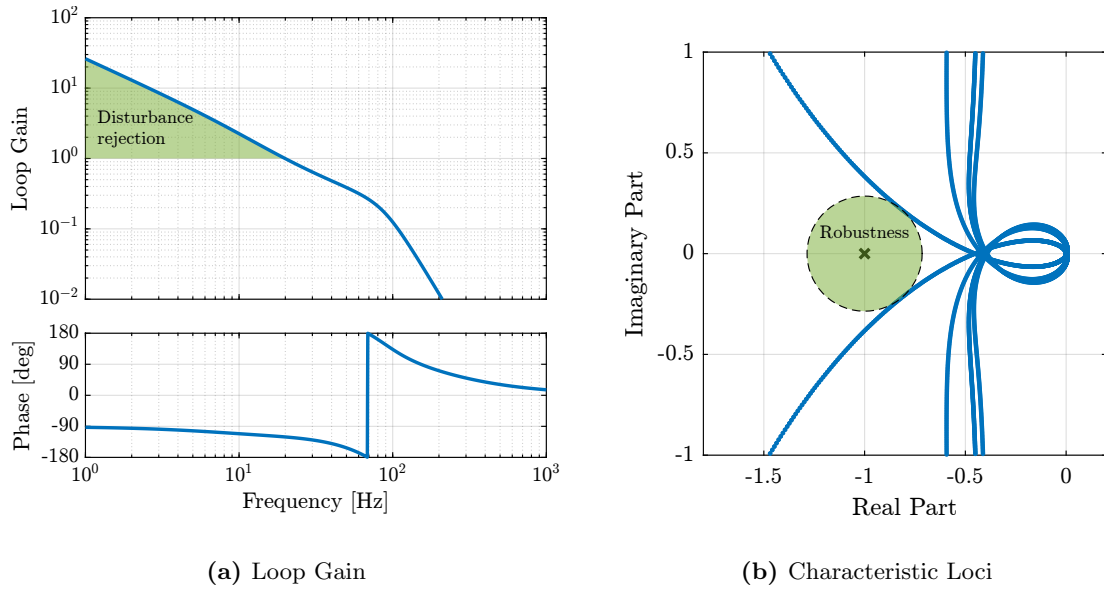


Figure 4.8: Decentralized HAC-IFF. Loop gain (a) is used for the design of the controller and to estimate the disturbance rejection performances. Characteristic Loci (b) is used to verify the stability and robustness of the feedback loop.

Feedback for active damping. The collocated nature of the force sensors ensures stability despite strong coupling between struts at resonance frequencies, enabling effective damping of structural modes. The outer loop implements High Authority Control, enabling precise positioning of the mobile platform.

Conclusion

After evaluating various architectures, the Stewart platform was selected for the active platform. The parallel kinematic structure offers superior dynamical characteristics, and its compact design satisfies the strict space constraints of the NASS. The extensive literature on Stewart platforms, including kinematic analysis, dynamic modeling and control, provides a robust theoretical foundation for this choice.

A configurable multi-body model of the Stewart platform was developed and validated against analytical equations. The modular nature of the model allows for progressive refinement of individual components (plates, joints and actuators) and geometry, making it a valuable tool throughout the development process. The validated model will be integrated into the broader multi-body representation of the micro-station, enabling comprehensive analysis of the complete NASS.

The use of this model extends beyond the current conceptual phase. It will serve as a crucial tool during the detailed design phase, where it will be used to optimize the design and guide the development of sophisticated control strategies. Furthermore, during the experimental phase, it will provide a theoretical framework for comparing and understanding measured dynamics.

The control aspects of the Stewart platform were addressed with particular attention to the challenges posed by its multi-input multi-output nature. Although the coupled dynamics of the system suggest the potential benefit of advanced control strategies, a simplified architecture was proposed for the validation of the NASS concept. This approach combines decentralized Integral Force Feedback for active damping with High Authority Control for positioning, which was implemented in the strut space to leverage the natural decoupling observed at low frequencies.

This study establishes the theoretical framework necessary for the subsequent development and validation of the NASS.

Bibliography

- [1] E. Nazaretski, K. Lauer, H. Yan, et al., “Pushing the limits: An instrument for hard x-ray imaging below 20 nm,” *Journal of Synchrotron Radiation*, vol. 22, no. 2, pp. 336–341, 2015 (cit. on pp. 5–7).
- [2] R. R. Geraldès, G. B. Z. L. Moreno, F. R. Lena, et al., “The high-dynamic cryogenic sample stage for sapoti/carnaúba at sirius/lms,” in *PROCEEDINGS OF THE 15TH INTERNATIONAL CONFERENCE ON X-RAY MICROSCOPY - XRM2022*, - 2023, nil (cit. on pp. 5, 6).
- [3] F. Villar, L. Andre, R. Baker, et al., “Nanopositioning for the esrf id16a nano-imaging beamline,” *Synchrotron Radiation News*, vol. 31, no. 5, pp. 9–14, 2018 (cit. on pp. 5, 6).
- [4] A. Schropp, R. Döhrmann, S. Botta, et al., “Ptydami: Ptychographic nano-analytical microscope,” *Journal of Applied Crystallography*, vol. 53, no. 4, pp. 957–971, 2020 (cit. on pp. 5, 6).
- [5] C. G. Schroer, M. Seyrich, M. Kahnt, et al., “Ptydami: Ptychographic nano-analytical microscope at petra iii: Interferometrically tracking positions for 3d x-ray scanning microscopy using a ball-lens retroreflector,” in *X-Ray Nanoimaging: Instruments and Methods III*, Sep. 2017 (cit. on pp. 5, 6).
- [6] M. Holler, J. Raabe, R. Wepf, et al., “Omny pin-a versatile sample holder for tomographic measurements at room and cryogenic temperatures,” *Review of Scientific Instruments*, vol. 88, no. 11, p. 113 701, 2017 (cit. on p. 6).
- [7] M. Holler, J. Raabe, A. Diaz, et al., “Omny-a tomography nano cryo stage,” *Review of Scientific Instruments*, vol. 89, no. 4, p. 043 706, 2018 (cit. on p. 6).
- [8] T. Stankevic, C. Engblom, F. Langlois, et al., “Interferometric characterization of rotation stages for x-ray nanotomography,” *Review of Scientific Instruments*, vol. 88, no. 5, p. 053 703, 2017 (cit. on p. 6).
- [9] C. Engblom et al., “Nanoprobe results: Metrology & control in stacked closed-loop systems,” in *Proc. of International Conference on Accelerator and Large Experimental Control Systems (ICALPCS’17)*, JACoW, Jan. 2018 (cit. on p. 6).
- [10] E. Nazaretski, D. S. Coburn, W. Xu, et al., “A new kirkpatrick-baez-based scanning microscope for the submicron resolution x-ray spectroscopy (srx) beamline at nsls-ii,” *Journal of Synchrotron Radiation*, vol. 29, no. 5, pp. 1284–1291, 2022 (cit. on p. 6).
- [11] J. Kelly, A. Male, N. Rubies, et al., “The delta robot-a long travel nano-positioning stage for scanning x-ray microscopy,” *Review of Scientific Instruments*, vol. 93, no. 4, nil, 2022 (cit. on p. 6).
- [12] T. Dehaeze, M. M. Mattenet, and C. Collette, “Sample stabilization for tomography experiments in presence of large plant uncertainty,” in *MEDSI’18*, (Paris, France), ser. Mechanical Engineering Design of Synchrotron Radiation Equipment and Instrumentation, Geneva, Switzerland: JACoW Publishing, Dec. 2018, pp. 153–157 (cit. on p. 6).
- [13] T. Dehaeze, J. Bonnefoy, and C. Collette, “Mechatronics approach for the development of a nano-active-stabilization-system,” in *MEDSI’20*, (Chicago, USA), ser. Mechanical Engineering Design of Synchrotron Radiation Equipment and Instrumentation, JACoW Publishing, 2021 (cit. on p. 6).
- [14] H. Taghirad, *Parallel robots : mechanics and control*. Boca Raton, FL: CRC Press, 2013 (cit. on p. 7).

- [15] W. Dong, L. Sun, and Z. Du, “Design of a precision compliant parallel positioner driven by dual piezoelectric actuators,” *Sensors and Actuators A: Physical*, vol. 135, no. 1, pp. 250–256, 2007 (cit. on p. 7).
- [16] Y. Shen, X. Luo, S. Wang, and X. Li, “Dynamic analysis of a 5-dof flexure-based nanopositioning stage,” *Mathematical Problems in Engineering*, vol. 2019, no. 1, nil, 2019 (cit. on pp. 7, 8).
- [17] B. J. Kenton and K. K. Leang, “Design and control of a three-axis serial-kinematic high-bandwidth nanopositioner,” *IEEE/ASME Transactions on Mechatronics*, vol. 17, no. 2, pp. 356–369, 2012 (cit. on p. 8).
- [18] A. Abu Hanieh, M. Horodincu, and A. Preumont, “Stiff and soft stewart platforms for active damping and active isolation of vibrations,” in *Actuator 2002, 8th International Conference on New Actuators*, 2002 (cit. on p. 8).
- [19] A. A. Hanieh, “Active isolation and damping of vibrations via stewart platform,” Ph.D. dissertation, Université Libre de Bruxelles, Brussels, Belgium, 2003 (cit. on p. 8).
- [20] A. Preumont, M. Horodincu, I. Romanescu, et al., “A six-axis single-stage active vibration isolator based on stewart platform,” *Journal of Sound and Vibration*, vol. 300, no. 3-5, pp. 644–661, 2007 (cit. on pp. 8, 22).
- [21] K. Furutani, M. Suzuki, and R. Kudoh, “Nanometre-cutting machine using a stewart-platform parallel mechanism,” *Measurement Science and Technology*, vol. 15, no. 2, pp. 467–474, 2004 (cit. on p. 8).
- [22] A. Preumont, *Vibration Control of Active Structures - Fourth Edition* (Solid Mechanics and Its Applications). Springer International Publishing, 2018 (cit. on p. 8).
- [23] D. Stewart, “A platform with six degrees of freedom,” *Proceedings of the institution of mechanical engineers*, vol. 180, no. 1, pp. 371–386, 1965 (cit. on p. 9).
- [24] B. Afzali-Far and P. Lidström, “On the inertia matrix of hexapod struts in the joint-space,” *To be submitted*, 2016 (cit. on p. 17).
- [25] Y. Chen and J. McInroy, “Decoupled control of flexure-jointed hexapods using estimated joint-space mass-inertia matrix,” *IEEE Transactions on Control Systems Technology*, vol. 12, no. 3, pp. 413–421, 2004 (cit. on p. 17).
- [26] J. McInroy and J. Hamann, “Design and control of flexure jointed hexapods,” *IEEE Transactions on Robotics and Automation*, vol. 16, no. 4, pp. 372–381, 2000 (cit. on p. 17).
- [27] J. McInroy, “Modeling and design of flexure jointed stewart platforms for control purposes,” *IEEE/ASME Transactions on Mechatronics*, vol. 7, no. 1, pp. 95–99, 2002 (cit. on p. 17).
- [28] A. Preumont, B. De Marneffe, and S. Krenk, “Transmission zeros in structural control with collocated multi-input/multi-output pairs,” *Journal of guidance, control, and dynamics*, vol. 31, no. 2, pp. 428–432, 2008 (cit. on p. 27).
- [29] S. Skogestad and I. Postlethwaite, *Multivariable Feedback Control: Analysis and Design - Second Edition*. John Wiley, 2007 (cit. on p. 29).